

Upcycling the carbon emissions from the steel industry into chemicals using three metal oxide loops

Varun Singh, Lukas C. Buelens, Hilde Poelman, Mark Saeys, Guy B. Marin, Vladimir V. Galvita

Supplementary Information (SI)

1 Calculations

1.1 Thermodynamic calculations

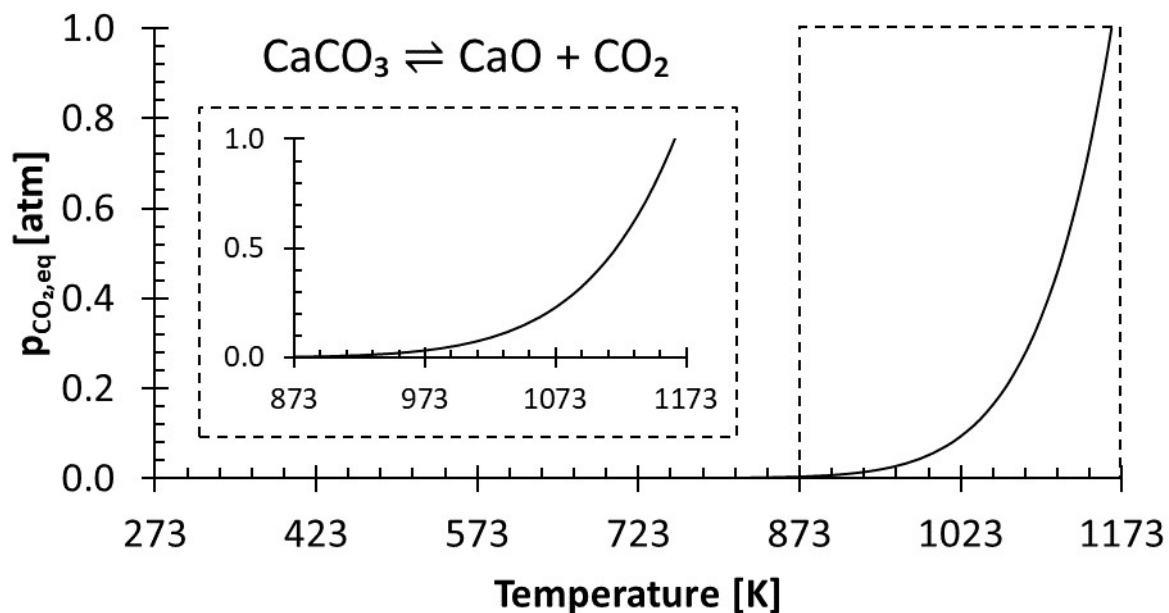


Figure S1: The variation of the thermodynamic equilibrium partial pressure of CO₂ against temperature at a pressure of 101.3 kPa. Data for CaO and CO₂ from NIST¹ and of CaCO₃ from FactSage (FactPS database)².

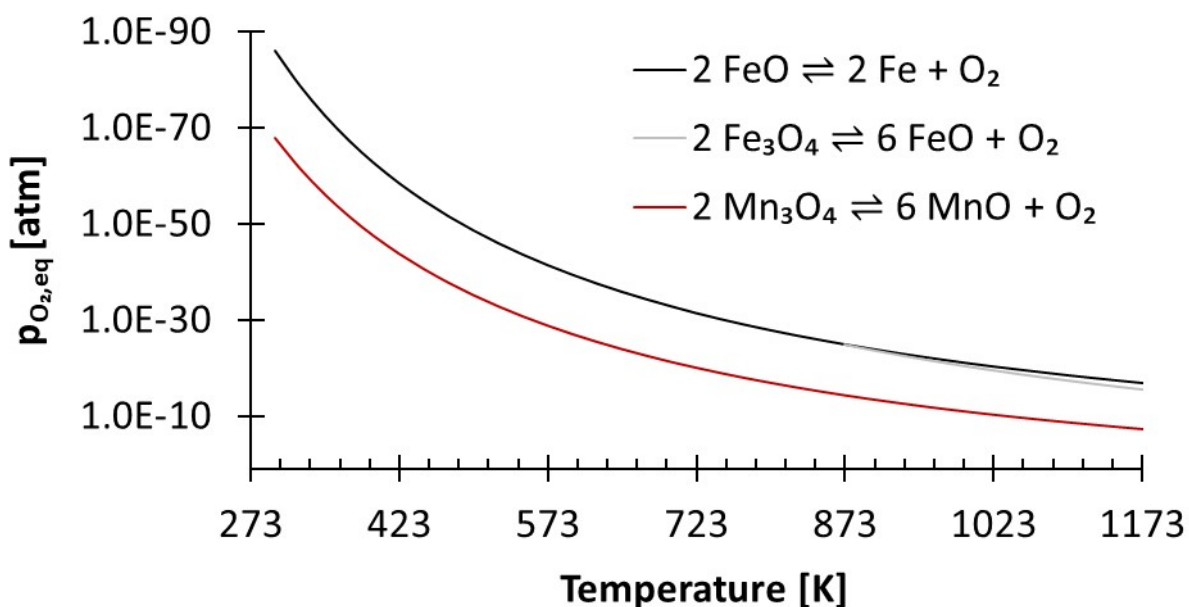


Figure S2: The variation of the thermodynamic equilibrium partial pressure of O₂ against temperature at a pressure of 101.3 kPa. Note that FeO is unstable below 843 K. Data for Fe₃O₄, Fe, and O₂ from NIST¹ and of FeO, Mn₃O₄, and MnO from FactSage (FactPS database)².

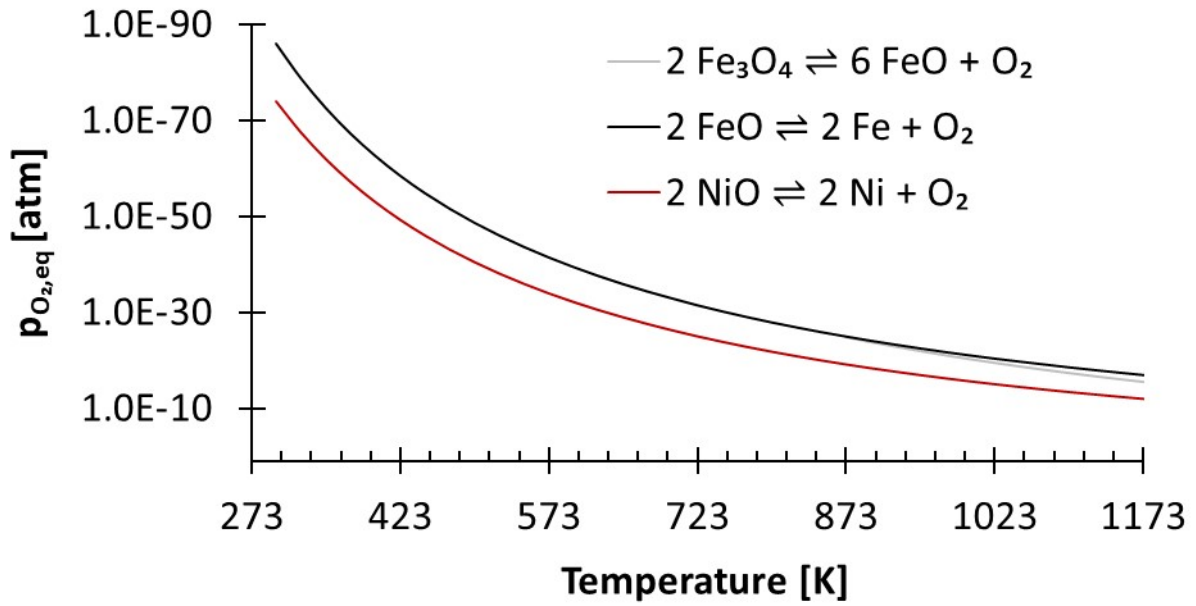


Figure S3: The variation of the thermodynamic equilibrium partial pressure of O_2 against temperature at a pressure of 101.3 kPa. Note that FeO is unstable below 843 K. Data for Fe_3O_4 , Ni, Fe, and O_2 from NIST¹ and of FeO and NiO from FactSage (FactPS database)².

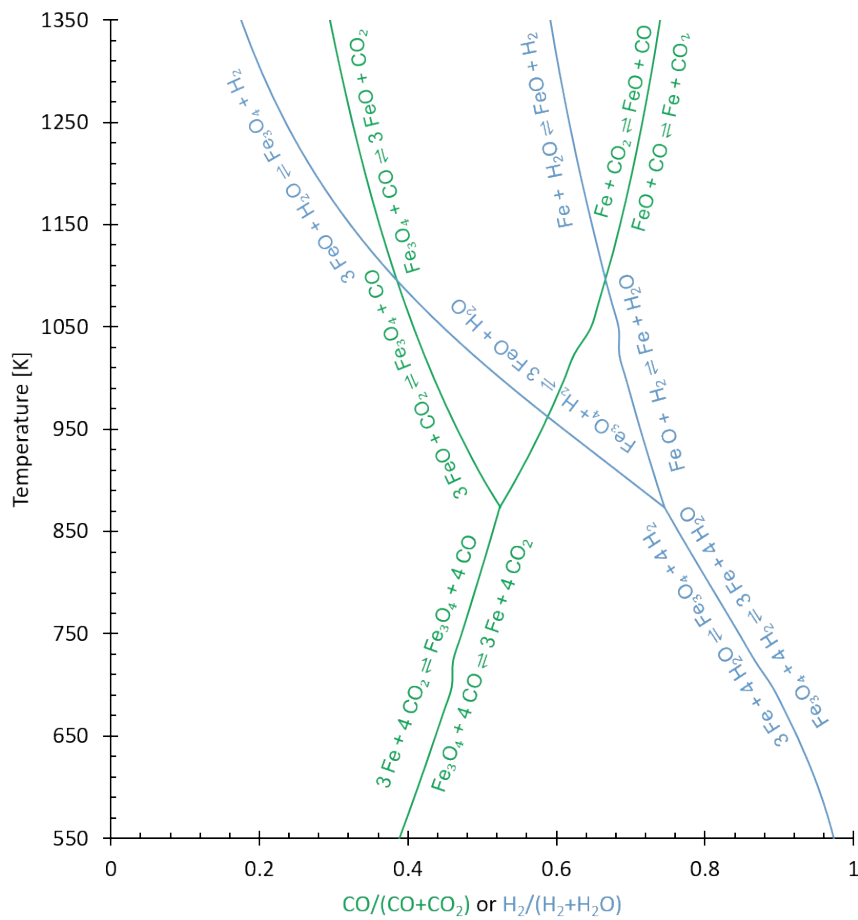


Figure S4: Bauer-Glaessner diagram generated using data from NIST¹ and FactSage (for FeO only).

1.2 Process simulations

Table S1: Aspen Plus® setup of modules, property methods, material databanks, and models.

Flowsheet setup	
Property method	<i>PR-BM</i> and <i>STEAM-TA</i> for free water method
Databank	<i>PURE36, INORGANIC, SOLIDS</i>
Solid components	C (graphite), Fe ₃ O ₄ , FeO, Fe, CaO, CaCO ₃ , Mn ₃ O ₄ , MnO, MgAl ₂ O ₄ , CeO ₂
Fluid components	CO, CO ₂ , H ₂ , H ₂ O, CH ₄ , O ₂ , N ₂
Stream class	<i>MIXCISLD</i>
Unit operation models	
Reactors	RGIBBS (by product distribution achieved minimisation of Gibbs free energy of selected solids and gases i.e. all possible components)
Separators	<i>SSplit</i> for solids and gases and <i>Sep</i> for separating gas mixtures
Fluid flow splitting	<i>FSplit</i>
Heat exchangers	<i>HeatX</i> (Shortcut method: 10 K minimum temperature approach and 10 K difference between hot inlet/cold outlet or hot outlet-cold inlet) and <i>Heater</i>
Mechanical operation models	
Compressor or turbine	<i>Compr</i> (72% isentropic efficiency & 100% mechanical efficiency)

For the process simulations, the C_p data for Fe₃O₄, Fe, and CaO were taken from NIST¹ and for FeO and CaCO₃ from FactSage (database: Fact-PS)².

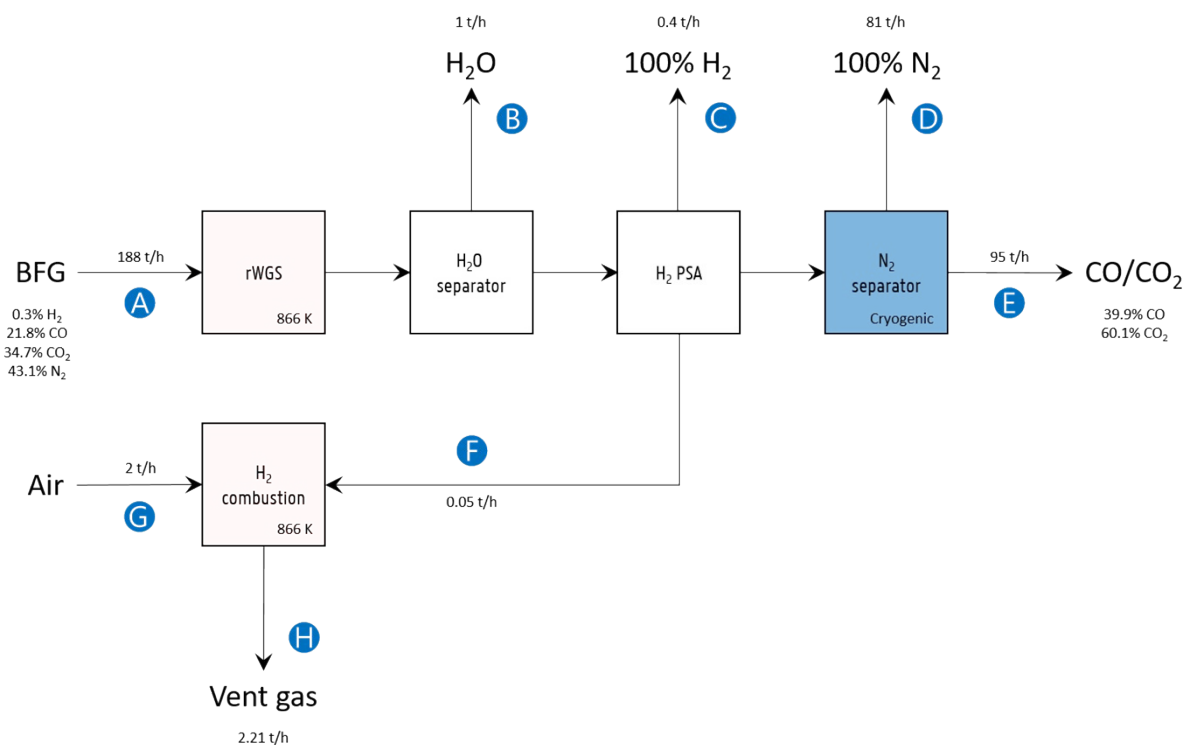


Figure S5: Block flow diagram of the process involving steady-state catalytic rWGS and downstream separation with mass flow rates. Labels: A: BFG feed to the catalytic reverse water-gas shift reaction (rWGS) block for producing a CO/CO₂ product stream E, B: a hypothetical H₂O separator (for example, a knockout drum), C: an H₂ pressure swing adsorption (PSA) column for creating a 100% pure H₂ stream partly for sale and partly for providing heat to the rWGS block (F), D: a pure N₂ stream generated from the product stream via cryogenic distillation, G: air fed for H₂ combustion, and H: outlet gas from H₂ combustion.

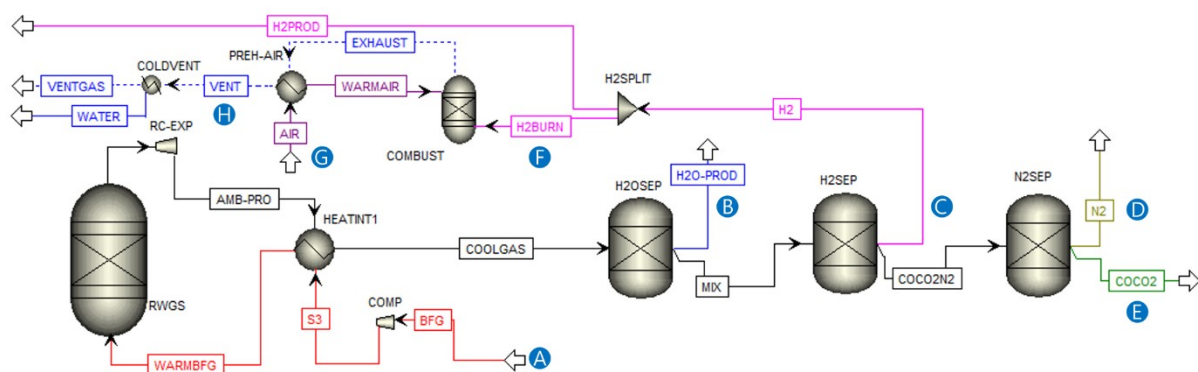


Figure S6: Aspen Plus flowsheet of rWGS with downstream separation. The alphabetical blue labels correspond to those from Figure S5.

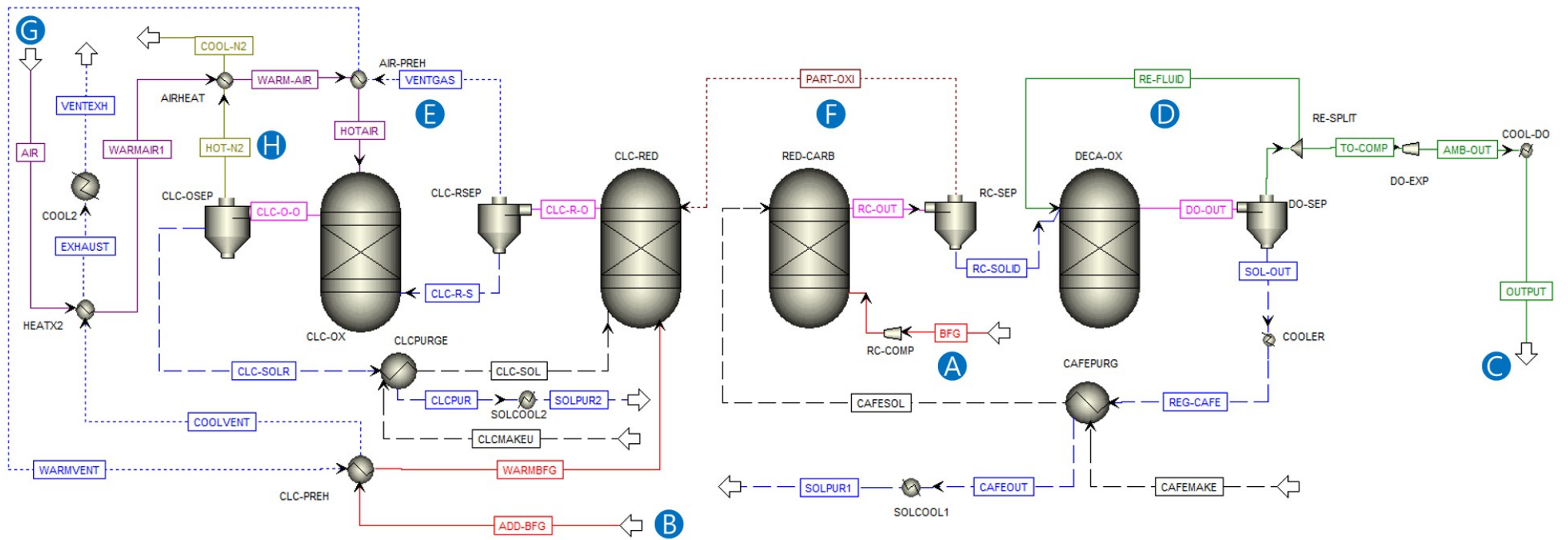


Figure S7: Aspen Plus flowsheet of the proposed chemical looping process. The alphabetical blue labels correspond to those from Figure 2 of the main text.

1.3 Techno-economic evaluation

1.3.1 Estimation of the costs of fresh and spent solids and catalyst

The costs of the precursors necessary for the preparation of the oxygen carriers, 80% $\text{Mn}_2\text{O}_3/\text{MgAl}_2\text{O}_4$ and 50% $\text{Fe}_2\text{O}_3/\text{MgAl}_2\text{O}_4$ and the CO_2 carrier 83% CaO/CeO_2 were calculated by extrapolating their costs from commercial suppliers in Belgium using the relation described in equation (S1)³, where $p(q)$ is the unit price of the precursor which is dependent on the quantity q , b is the scale parameter and γ is the discount factor.

$$p(q) = b * q^\gamma \quad (\text{S1})$$

Figure S8, Figure S9, and Figure S10 show the retail prices used for the different precursors or raw materials used for the synthesis of the oxygen carriers and the CO_2 carrier. The cost of water used in the synthesis was assumed to be 0.79 EUR₂₀₂₀/tonne based on the prices in the Netherlands⁴, which is a conservative estimate when compared to 0.10 EUR₂₀₁₅/tonne made by Cormos⁵.

Assuming that orders are made around 2 to 4 times a year⁶, the order size for 80% $\text{Mn}_2\text{O}_3/\text{MgAl}_2\text{O}_4$ is 500 tonnes for consumption of around 1000 tonnes/year, for 50% $\text{Fe}_2\text{O}_3/\text{MgAl}_2\text{O}_4$ it is 1000 tonnes for consumption of around 5000 tonnes/year, and for the CO_2 sorbent 83% CaO/CeO_2 10000 tonnes for consumption of around 78000 tonnes/year. This corresponds to a synthesis campaign length (inclusive of 1 day for cleaning) of 4 days for 80% $\text{Mn}_2\text{O}_3/\text{MgAl}_2\text{O}_4$, 8 days for 50% $\text{Fe}_2\text{O}_3/\text{MgAl}_2\text{O}_4$, and 71 days for 83% CaO/CeO_2 . Clearly, the synthesis of the CO_2 sorbent would benefit from a continuous production line and its procurement would require at least 2 suppliers because of the large quantities necessary. For all the materials, the production scale is large (>150 tonnes/day) and in the same order of magnitude as the production of zeolites for fluid catalytic cracking (FCC).

In Table S2, Table S3, and Table S4, it was assumed that 5% of the material is lost during the synthesis. The USD prices from mid-2017 were converted to 2020 were converted using the web tool by U.S. Bureau of Labor Statistics⁷ and a conversion factor of 1.06 USD₂₀₂₀ per 1 USD_{mid-2017}. Conversion of EUR to USD was carried out assuming that 0.9 EUR₂₀₂₀ was equivalent to 1 USD₂₀₂₀. The selling margin was calculated as a percentage of the pre-margin costs using equation (S2)⁶.

$$\text{Margin (\% of pre - margin costs)} = 60.976 * (\text{order size in tonnes})^{-0.28632} \quad (\text{S2})$$

The general and administrative costs amount to 5% of the subtotal and the sales, administrative, research, and distribution costs amount to 5% of the sum of the subtotal and the general and administrative costs⁶.

The oxygen carriers were synthesised via co-precipitation based on the recipe described by Dharanipragada et al.⁸. Co-precipitation was carried out by adding 28% $\text{NH}_4\text{OH}/\text{H}_2\text{O}$ to a 2 M nitrate solution of the appropriate metal precursors. The CO_2 carrier, 83% CaO/CeO_2 was synthesised via a

wet physical mixing route using calcium d-gluconate monohydrate and cerium nitrate hexahydrate with deionised water as solvent based on the work by Liu et al.⁹.

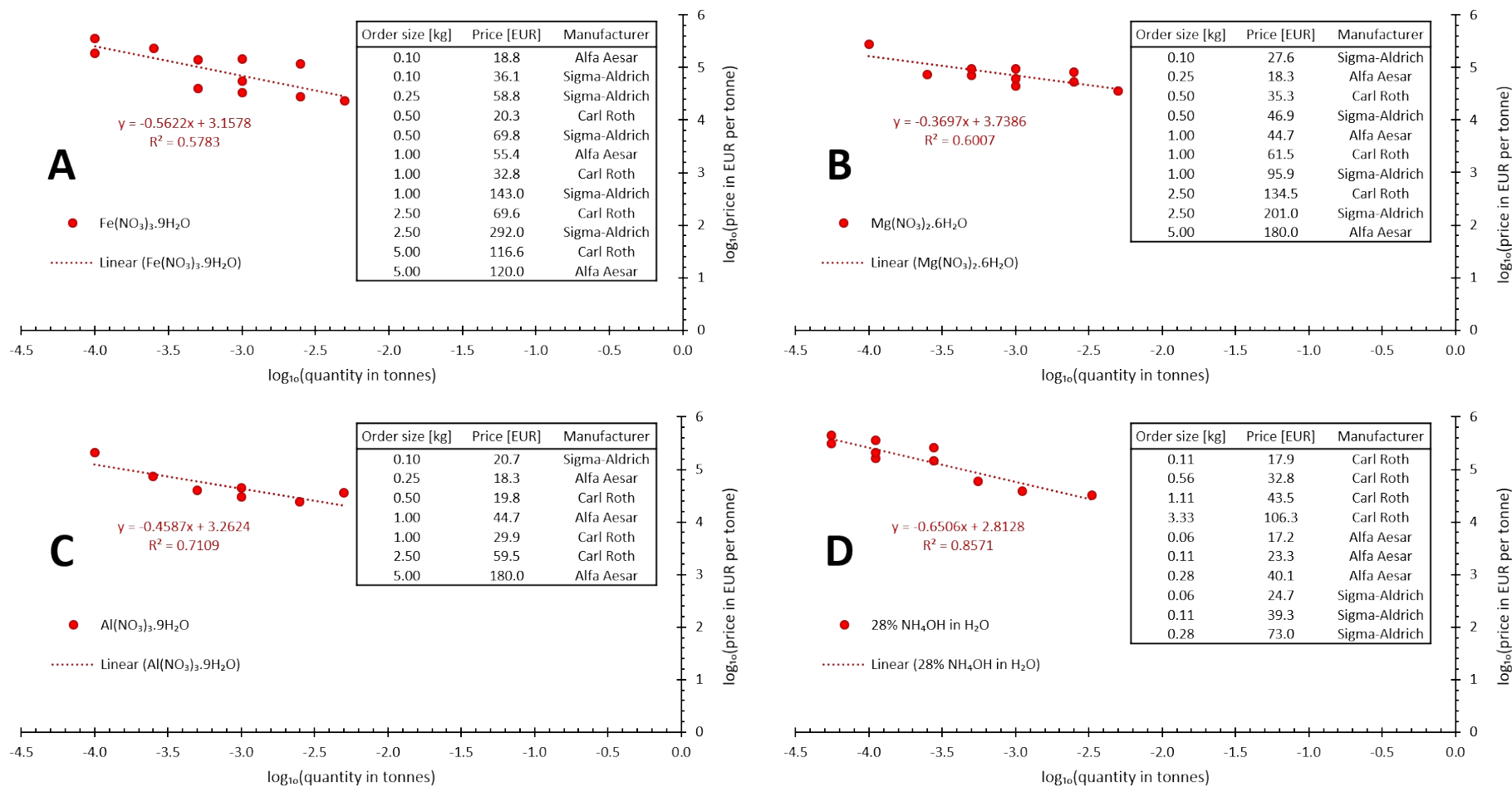


Figure S8: Fit of retail pricing data obtained from Sigma-Aldrich (Belgium), Carl Roth (Belgium), and Alfa Aesar (Germany) on 04/06/2021 and 05/06/2021 for A: iron nitrate nonahydrate, B: magnesium nitrate hexahydrate, C: aluminium nitrate nonahydrate, and D: 28% NH₄OH in H₂O, precursors for the synthesis of 50% Fe₂O₃/MgAl₂O₄. The purity of precursors was higher than 98% for all considered data points.

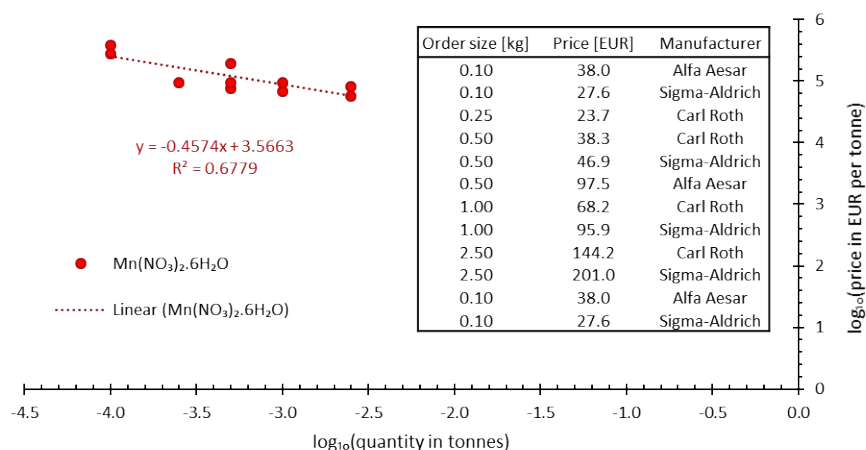


Figure S9: Fit of retail pricing data obtained from Sigma-Aldrich (Belgium), Carl Roth (Belgium), and Alfa Aesar (Germany) on 04/06/2021 and 05/06/2021 for manganese nitrate hexahydrate, precursor for the synthesis of 80% $Mn_2O_3/MgAl_2O_4$. The purity of the precursor was higher than 98% for all considered data points.

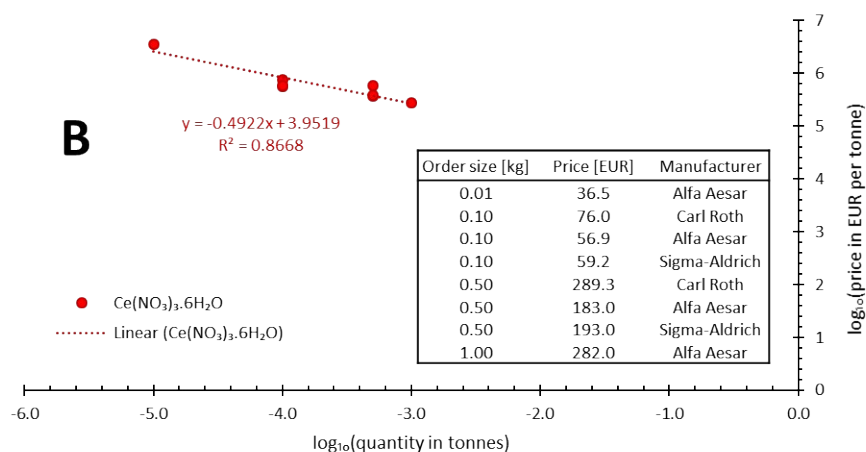
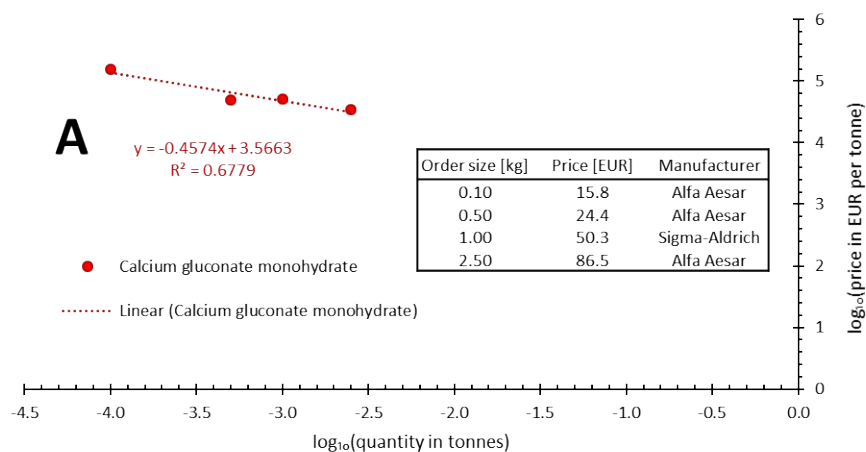


Figure S10: Fit of retail pricing data obtained from Sigma-Aldrich (Belgium), Carl Roth (Belgium), and Alfa Aesar (Germany) on 04/06/2021 and 05/06/2021 for A: calcium gluconate monohydrate and B: cerium nitrate hexahydrate, precursor for the synthesis of 83% CaO/CeO_2 . The purity of precursors was higher than 98% for all considered data points.

Table S2: Cost estimation for preparing 80% Mn₂O₃/MgAl₂O₄ via co-precipitation.

Material Costs			
Precursor	Cost [EUR/tonne]	kg/kg of oxygen carrier	EUR/tonne of oxygen carrier
Mn(NO ₃) ₂ ·6H ₂ O	2.73	135.5	370
Mg(NO ₃) ₂ ·6H ₂ O	0.44	746.4	328
Al(NO ₃) ₃ ·9H ₂ O	1.30	93.9	122
28% NH ₄ OH in H ₂ O	4.69	4.2	20
H ₂ O	18.72	0.8	15
Total			854
Costs of synthesis steps			
Step with a brief <i>description</i>	EUR/hours		EUR/day
Reactor, mixing <i>To mix precursors during co-precipitation</i>	191		4579
Filter, rotary vacuum <i>To filter precipitate</i>	286		6869
Dryer, rotary (100 – 300°C) <i>To dry the precipitate</i>	286		6869
Kiln, continuous indirect (100 – 1290°C) <i>To calcine the material</i>	310		7441
Scrubber for NO _x emissions <i>To avoid emissions from calcination</i>	191		4579
Total			30340
Synthesis campaign costs			
Order size [tonnes]			500
Cost of synthesis steps [EUR/day]			30340
Campaign length [days]			4
Campaign cost [EUR]			121350
Campaign cost [EUR/tonne _{product}]			243
Subtotal before Overhead and Margin			
Materials cost [EUR/tonne _{product}]			854
Campaign cost [EUR/tonne _{product}]			243
Subtotal [EUR/tonne _{product}]			1097
Overhead and Margin			
General and administrative costs [EUR/tonne _{product}]			55
Sales, administrative, research, and distribution costs [EUR/tonne _{product}]			58
Margin [EUR/tonne _{product}]			124
Total estimated price			
Estimated price [EUR/tonne _{product}]			1333

Table S3: Cost estimation for preparing 50% Fe₂O₃/MgAl₂O₄ via co-precipitation.

Material Costs			
Precursor	Cost [EUR/tonne]	kg/kg of oxygen carrier	EUR/tonne of oxygen carrier
Fe(NO ₃) ₃ ·9H ₂ O	2.72	16.9	46
Mg(NO ₃) ₂ ·6H ₂ O	1.10	411.7	452
Al(NO ₃) ₃ ·9H ₂ O	3.24	44.9	146
28% NH ₄ OH in H ₂ O	7.20	2.0	14
H ₂ O	28.77	0.8	23
Total			680
Costs of synthesis steps			
Step with a brief <i>description</i>	EUR/hours		EUR/day
Reactor, mixing <i>To mix precursors during co-precipitation</i>	191		4579
Filter, rotary vacuum <i>To filter precipitate</i>	286		6869
Dryer, rotary (100 – 300°C) <i>To dry the precipitate</i>	286		6869
Kiln, continuous indirect (100 – 1290°C) <i>To calcine the material</i>	310		7441
Scrubber for NO _x emissions <i>To avoid emissions from calcination</i>	191		4579
Total			30340
Synthesis campaign costs			
Order size [tonnes]			1000
Cost of synthesis steps [EUR/day]			30340
Campaign length [days]			8
Campaign cost [EUR]			242700
Campaign cost [EUR/tonne _{product}]			243
Subtotal before Overhead and Margin			
Materials cost [EUR/tonne _{product}]			680
Campaign cost [EUR/tonne _{product}]			243
Subtotal [EUR/tonne _{product}]			923
Overhead and Margin			
General and administrative costs [EUR/tonne _{product}]			46
Sales, administrative, research, and distribution costs [EUR/tonne _{product}]			48
Margin [EUR/tonne _{product}]			86
Total estimated price			
Estimated price [EUR/tonne _{product}]			1103

Table S4: Cost estimation for preparing 83% CaO/CeO₂ via wet physical mixing.

Material Costs			
Precursor	Cost [EUR/tonne]	kg/kg of CO ₂ carrier	EUR/tonne of CO ₂ carrier
Calcium gluconate monohydrate	7.13	10.7	77
Ce(NO ₃) ₃ ·6H ₂ O	0.46	141.5	65
H ₂ O	35.64	0.8	28
Total			169
Costs of synthesis steps			
Step with a brief <i>description</i>	EUR/hours		EUR/day
Mixer, slurry <i>To mix precursors and the thickening solution</i>	191		4579
Dryer, rotary (100 – 300°C) <i>To dry the formed gel</i>	286		6869
Kiln, continuous indirect (100 – 1290°C) <i>To calcine the material</i>	310		7441
Scrubber for NO _x emissions <i>To avoid emissions from calcination</i>	191		4579
Total			23470
Synthesis campaign costs			
Order size [tonnes]			10000
Cost of synthesis steps [EUR/day]			23470
Campaign length [days]			71
Campaign cost [EUR]			242700
Campaign cost [EUR/tonne _{product}]			167
Subtotal before Overhead and Margin			
Materials cost [EUR/tonne _{product}]			169
Campaign cost [EUR/tonne _{product}]			167
Subtotal [EUR/tonne _{product}]			336
Overhead and Margin			
General and administrative costs [EUR/tonne _{product}]			17
Sales, administrative, research, and distribution costs [EUR/tonne _{product}]			18
Margin [EUR/tonne _{product}]			16
Total estimated price			
Estimated price [EUR/tonne _{product}]			386

The price of 21% Ni/Al₂O₃ catalyst was obtained from Baddour et al.⁶ and then converted to the equivalent price of approximately 45000 EUR/tonne using a inflation factor of 1.06 USD₂₀₂₀ per 1 USD_{mid-2017} and 0.9 EUR₂₀₂₀ per 1 USD₂₀₂₀. It was assumed that Ni could be recovered from the spent catalyst at negligible cost and at the rate of 13770 EUR/tonne, based on the 10 year average price of nickel from 2010 to 2020 on London Metal Exchange and a conversion of USD to EUR at 0.9 EUR/USD. Using a similar approach, the value of spent iron-based oxygen carrier was estimated to be 92 EUR/tonne by assuming that the value of the spent iron-based oxygen carrier would be equal to that of iron ore. The value of spent manganese-based oxygen was assumed to be 4 EUR/tonne based on the 10 year average price of manganese ore and CNY to EUR exchange rate from 2010 to 2020 obtained from tradingeconomics.com¹⁰. Finally, the spent CO₂ carrier, 83% CaO/CeO₂, is assumed to have a value of 40 EUR₂₀₂₀/tonne (by taking into account the inflation)¹¹. Table S5 summarises the information in this paragraph.

Table S5: Price of the natural ores and the data sources.

	Cost [EUR ₂₀₂₀ /tonne]	Source
Iron ore	92	London Metal Exchange
Manganese ore	4	tradingeconomics.com ¹⁰
Limestone	40	Anantharaman et al. ¹¹
Nickel	13770	London Metal Exchange

1.4 Exergy and energy

To demonstrate the validity of the assumption that the electricity demand for cryogenic distillation can be approximated by equation (S3), we have computed the energy demand using the same approach for an air separation unit for which abundant data is available in literature^{5, 12, 13}. *Energy transfer* and *Heat duty* (given by equations (S5) and (S6)) determined by the so-called “distillation resistance” (Ω) (see equation (S4)) as defined by Lange¹⁴ are shown below.

$$\text{Electricity demand} = \text{Energy transfer} - \text{Heat duty} \quad (\text{S3})$$

$$\Omega \left(\frac{1}{^\circ\text{C}} \right) = 100 * \frac{w_{N_2}}{BP_{N_2} - BP_{O_2}} = \frac{0.77}{-183 - (-196)} = 6 \quad (\text{S4})$$

$$\text{Energy transfer} \left(\frac{\text{GJ}}{\text{tonne}_{\text{feed}}} \right) = 1.1 * \Omega = 6.6 \quad (\text{S5})$$

$$\text{Heat duty} \left(\frac{\text{GJ}}{\text{tonne}_{\text{feed}}} \right) = 0.57 * \Omega = 3.4 \quad (\text{S6})$$

Based on these, the electricity required for separating O₂ would be 3.2 GJ/t_{feed}, where feed is air composed of 79 mol% N₂ and 21 mol% O₂. Cormos⁵ reported power consumption of 225 kWh/t_{O₂}, corresponding to 3.5 GJ/tonne_{feed}. Castle¹³ has shown in 2002 that, over the years, the power consumption of ASU has consistently decreased and was expected to reach 0.3 kWh/Nm³ of low

pressure gaseous O₂ in 2010, corresponding to 3.2 GJ/tonne_{feed}. More recently (in 2014), Banaszkiwicz et al. reported a power consumption of 200 kWh/t_{O₂}, corresponding to 3.1 GJ/t_{feed}. In all cases, the value corresponds to the estimation made by equation (S3) within an error margin of ±10%.

To demonstrate that nullifying the carbon footprint of the proposed chemical looping process is far more facile than that of the rWGS reaction followed by downstream separation using mature technologies, equation (S7) developed by House et al.¹⁵ based on the Sherwood plot was proposed, where P is the price in \$/kg and C is the mass concentration.

$$P = 0.0208 * \left(\frac{1}{C}\right)^{0.5434} \quad (S7)$$

For a natural gas fired power plant with a CO₂ concentration of about 6.2% in the flue gas, the cost of CO₂ capture from equation (S7) is 94 \$/tonne. This corresponds well with the value of 72 \$₂₀₂₀/tonne reported by Smith et al.¹⁶, albeit a bit overestimated, but well within the range of 54 to 103 \$₂₀₂₀/tonne estimated by Dieterich et al.¹⁷ (assuming 1 EUR₂₀₂₀ = 1.142 USD₂₀₂₀). Applying the same equation to the vent gas from the chemical looping combustion section of the proposed scheme, the estimated value is 30 \$/tonne.

2 Experimental section

2.1 Characterisation of materials

2.1.1 N₂ sorption

Textural properties of the materials were analysed by sorption measurements with N₂ at 77 K in a Micromeritics Tristar II apparatus. Prior to the measurements, the materials were degassed overnight under an N₂ flow at 623 K in a Micromeritics SmartPrep apparatus. At least 69 points of relative pressure between 0.01 and 0.99 were measured to develop an adsorption-desorption isotherm. IUPAC guidelines were applied for estimating the specific surface area based on the Brunauer-Emmett-Teller theory¹⁸. Pore volume was measured at the highest relative pressure (approximately 0.99) during the adsorption phase. Average pore size was estimated using the Barrett-Joyner-Halenda (BJH) analysis applied to the desorption isotherm. Particle size was calculated using the relation described in the work by Wohlleben et al.¹⁹ and assuming that the particles were spherical and without internal pores. 100 to 400 mg of the samples were used for the measurements and at least 3 independent measurements were carried out for each sample. Error bars were generated using the standard deviation from the repeat measurements.

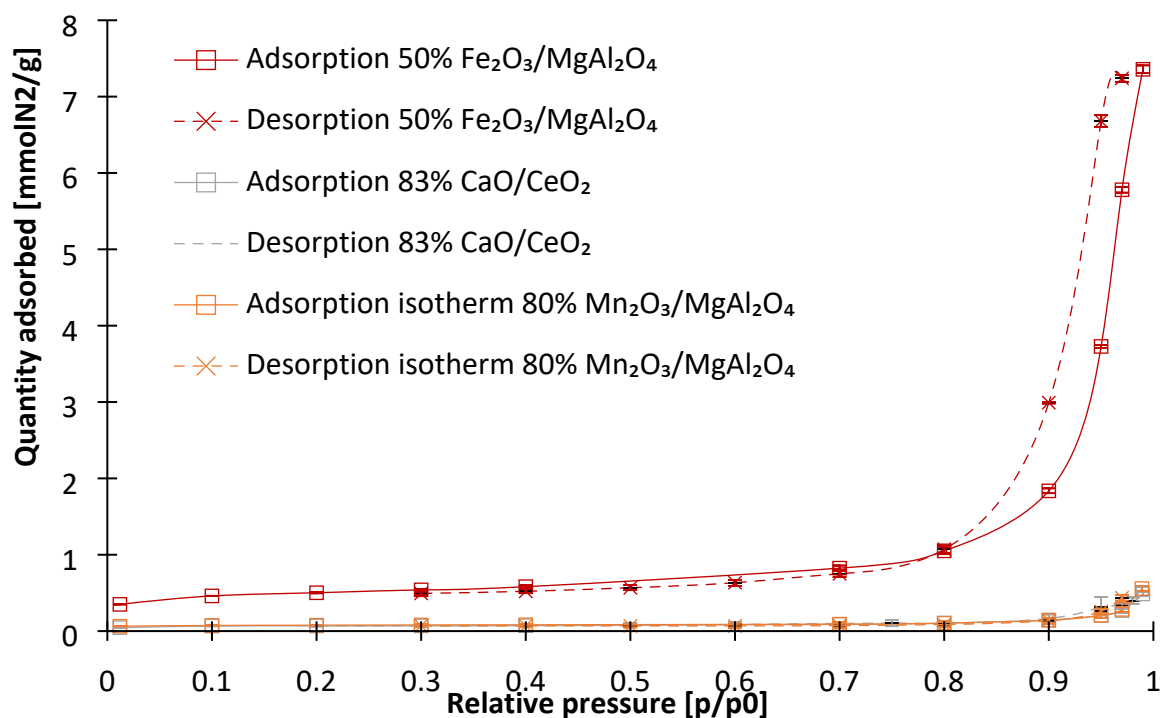


Figure S11: Nitrogen sorption isotherm of the oxygen carrier at 77 K. p_0 on the x-axis represents atmospheric pressure and p the pressure during the measurement. At least 69 measured points were interpolated to provide 22 common points at regular pressure intervals for the assessment of the standard deviation depicted by the error bars.

Based on the IUPAC classification¹⁸, the oxygen carrier, 50% Fe₂O₃/MgAl₂O₄, shows characteristics of a Type IV(a) isotherm with an H2(b) type hysteresis (Figure S11 – in red), indicating mesoporosity with a wide mesopore size distribution. The isotherms of the CO₂ carrier, 83% CaO/CeO₂ (Figure S11 – in grey) and the oxygen carrier, 80% Mn₂O₃/MgAl₂O₄ (Figure S11 – in orange) resemble a Type II isotherm with evidence of macroporosity and negligible mesoporosity. The quantified textural properties are displayed in Table S6.

Table S6: Textural properties of the as prepared materials from nitrogen sorption measurements at 77 K.

	50% Fe ₂ O ₃ /MgAl ₂ O ₄	83% CaO/CeO ₂	80% Mn ₂ O ₃ /MgAl ₂ O ₄
BET surface area [m²/g]	41.5 ± 0.3	6.3 ± 0.3	6.7 ± 0.2
Pore volume [10⁻⁹ m³/g]	258 ± 1	18 ± 1	20 ± 1
BJH desorption pore diameter [nm]	22.5 ± 0.2	32.7 ± 5.4	36.4 ± 4.3
Particle size [nm]	33 ± 0.3	237 ± 11.9	177 ± 4.3

2.1.2 Energy dispersive x-ray spectroscopy

SEM-EDX was performed on the as prepared OC and the CC to obtain their composition using a SEM JEOL JSM 5400 setup equipped with an INCA x-act extension (Oxford instruments) for Energy Dispersive X-ray spectrometry (EDX) measurements.

Table S7: Elemental composition using energy dispersive x-ray spectroscopy (EDX) or inductively coupled plasma coupled with optical emission spectroscopy (ICP-OES) expressed in mass percentage of the materials used for the experimental demonstration of the process concept. The error indicates the standard deviation based on at least four measurements. Values in brackets indicate expected values.

Element	50% Fe ₂ O ₃ /MgAl ₂ O ₄	80% Mn ₂ O ₃ /MgAl ₂ O ₄	83% CaO/CeO ₂ **
Fe	36 ± 2 (35)	-	-
Mn	-	54 ± 1 (56)	-
Ni	-	-	-
Mg	6 ± 1 (8)	3 ± 0 (3)	-
Al	17 ± 2 (19)	8 ± 1 (8)	-
Ca	-	-	74 ± 4 (81)
Ce	-	-	26 ± 4 (19)
O	40 ± 3 (37)	34 ± 1 (33)	-

** measurement on an oxygen free basis.

2.1.3 X-ray diffraction

Powder X-ray diffraction (XRD) measurements using Cu K α radiation (wavelength = 0.15406 nm) were performed with a Siemens Diffractometer Kristalloflex D5000. Diffractograms were collected between 2 θ angles of 5° and 110° with a step of 0.02° and 10 s collection time at each angle. The Rietveld refinement of the diffractogram was performed using GSAS²⁰ and EXPGUI²¹ to estimate the crystallite size and material composition. For quantification of the instrumental width, a reference LaB₆ (660a from NIST) measurement was used. The degree of crystallinity was estimated using equation (S8) upon obtaining its constituent terms from Rietveld refinement.

$$\text{Degree of crystallinity (vol\%)} = \frac{\text{Area under diffracted peaks}}{\text{Area under background} + \text{Area under diffracted peaks}} * 100 \quad (\text{S8})$$

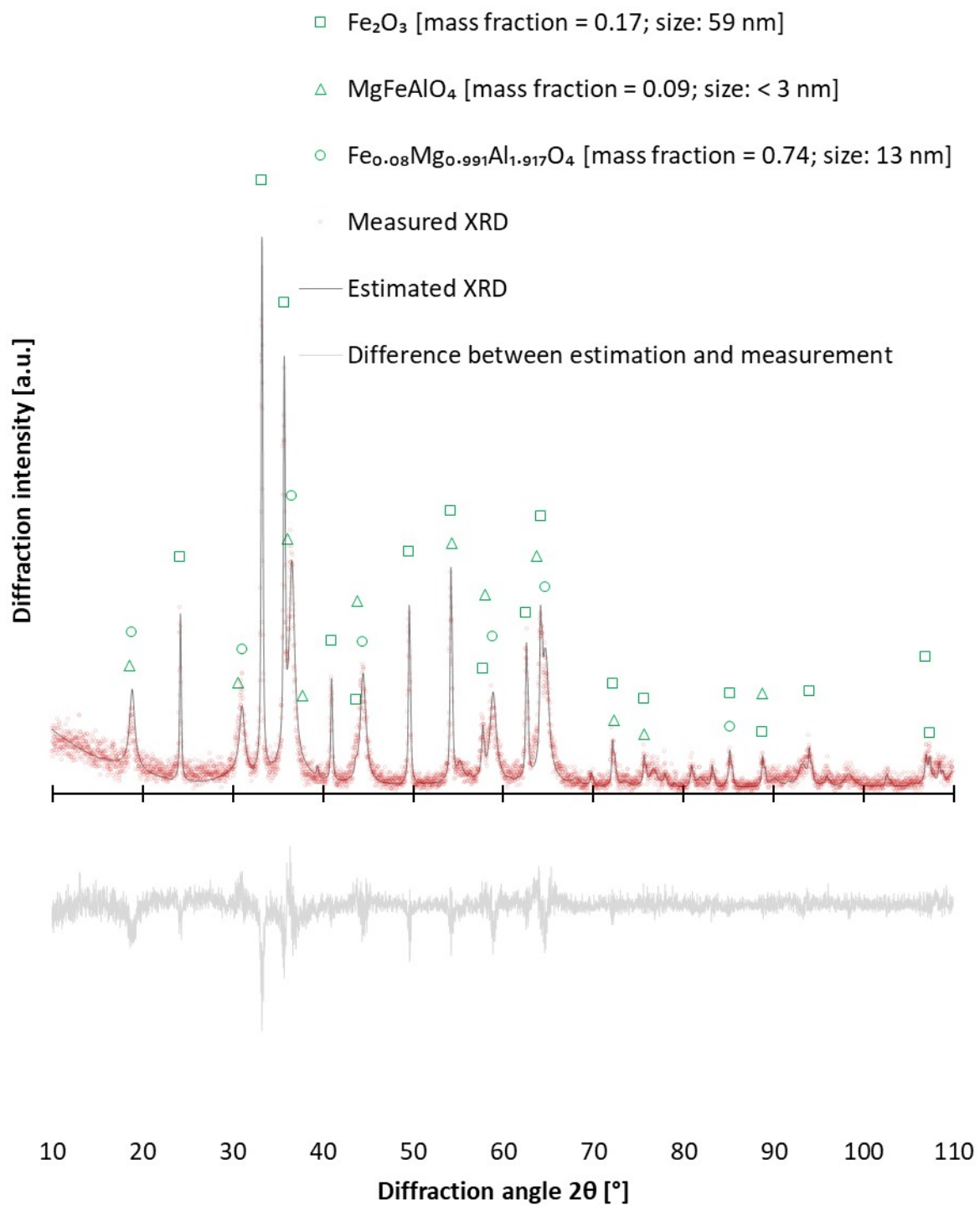


Figure S12: X-ray diffractogram of the calcined 50% $\text{Fe}_2\text{O}_3/\text{MgAl}_2\text{O}_4$ oxygen carrier (in red circles) with the X-ray diffractogram generated by Rietveld refinement (in black) and the difference between the observed and fitted

diffractogram (in grey, bottom). Peaks which have an intensity higher than 5% of the maximum peak intensity are marked and identified on the plot.

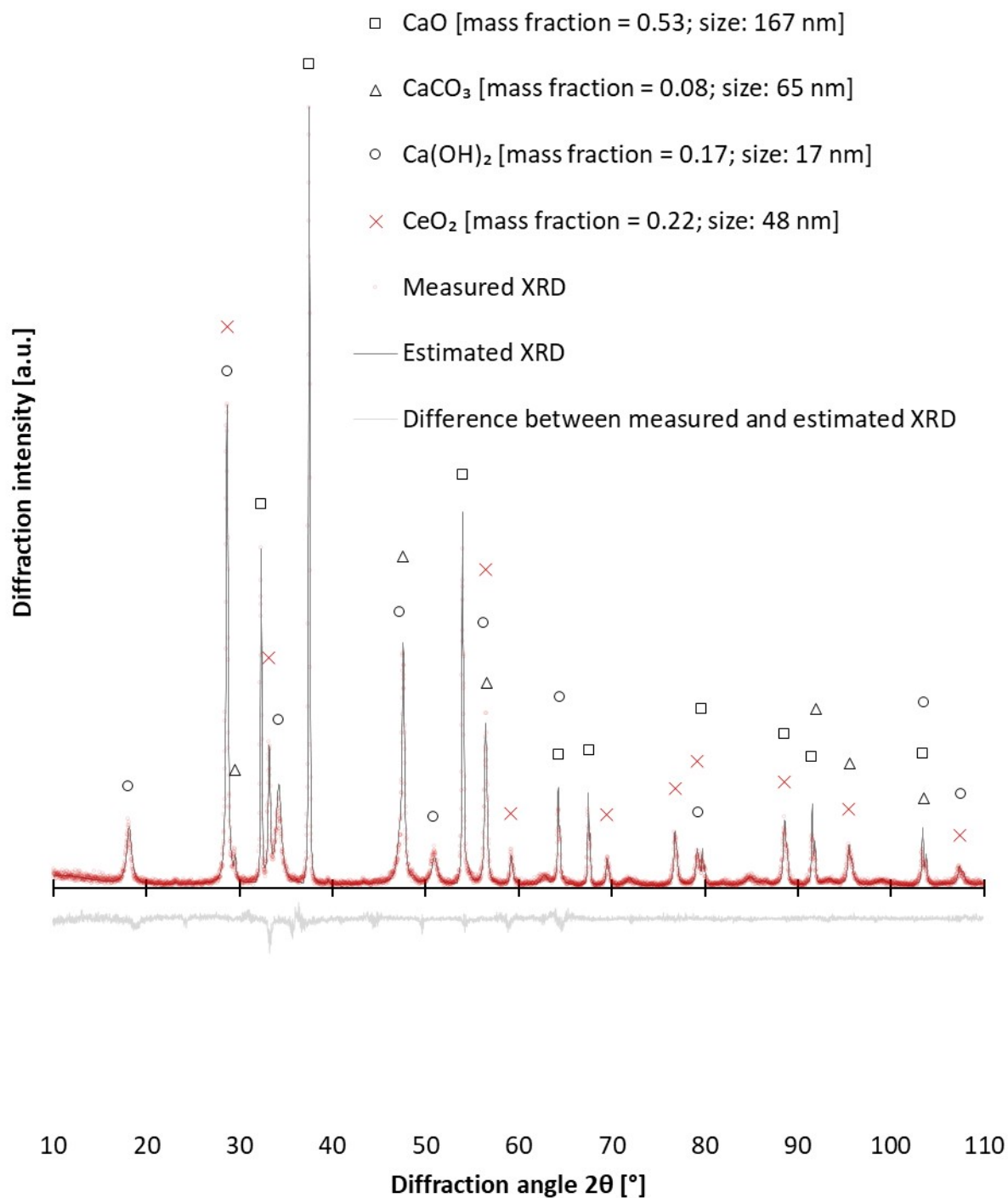


Figure S13: X-ray diffractogram of the calcined CO₂ carrier (in red circles) with the X-ray diffractogram generated by Rietveld refinement (in black) and the difference between the observed and fitted diffractogram (in grey, bottom). Peaks which have an intensity higher than 1% of the maximum peak intensity are marked and identified on the plot.

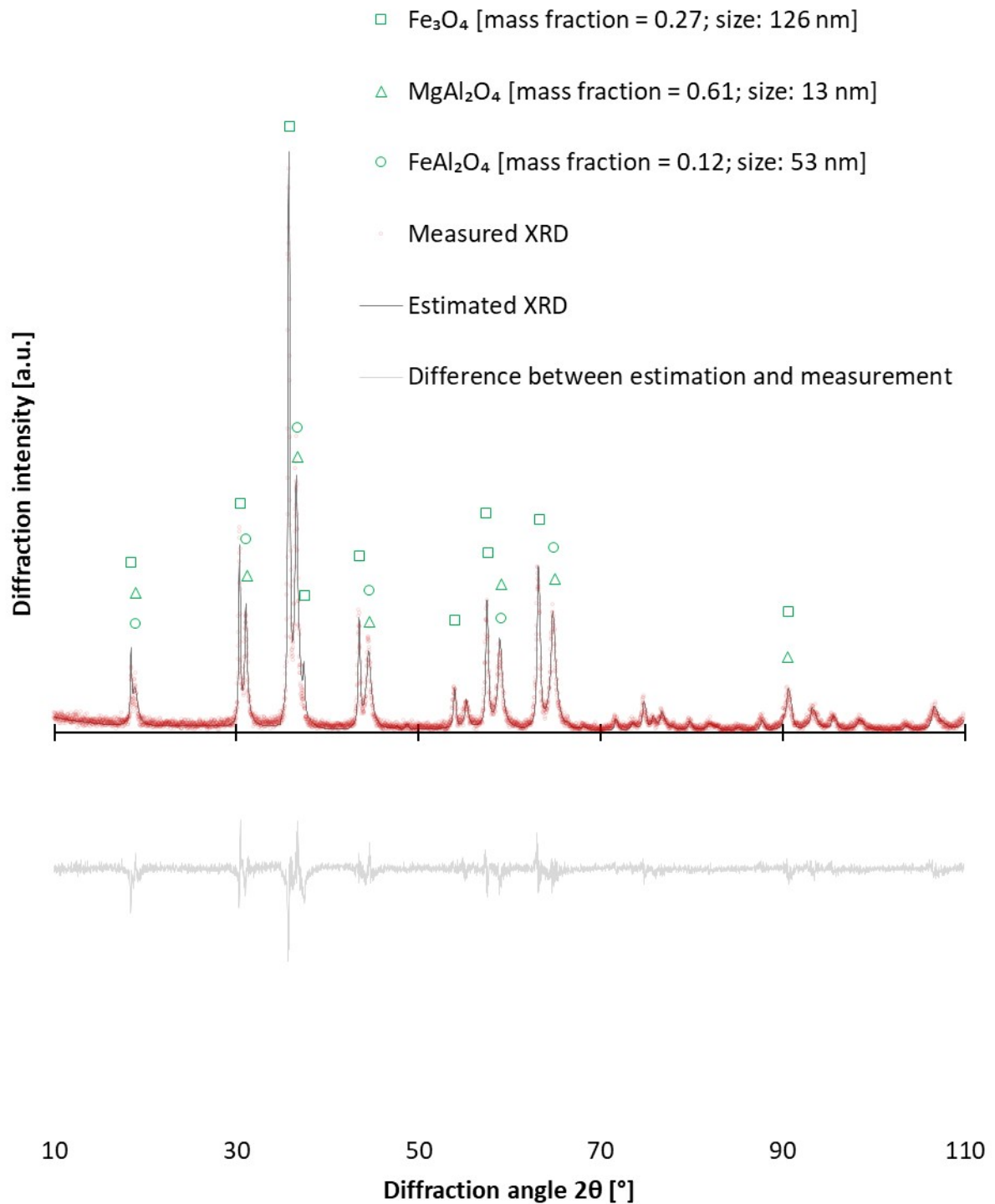


Figure S14: X-ray diffractogram of the oxygen carrier 50% $\text{Fe}_2\text{O}_3/\text{MgAl}_2\text{O}_4$ after being fully oxidised by CO_2 (in red circles) with the X-ray diffractogram generated by Rietveld refinement (in black) and the difference between the observed and fitted diffractogram (in grey, bottom). Peaks which have an intensity higher than 5% of the maximum peak intensity are marked and identified on the plot.

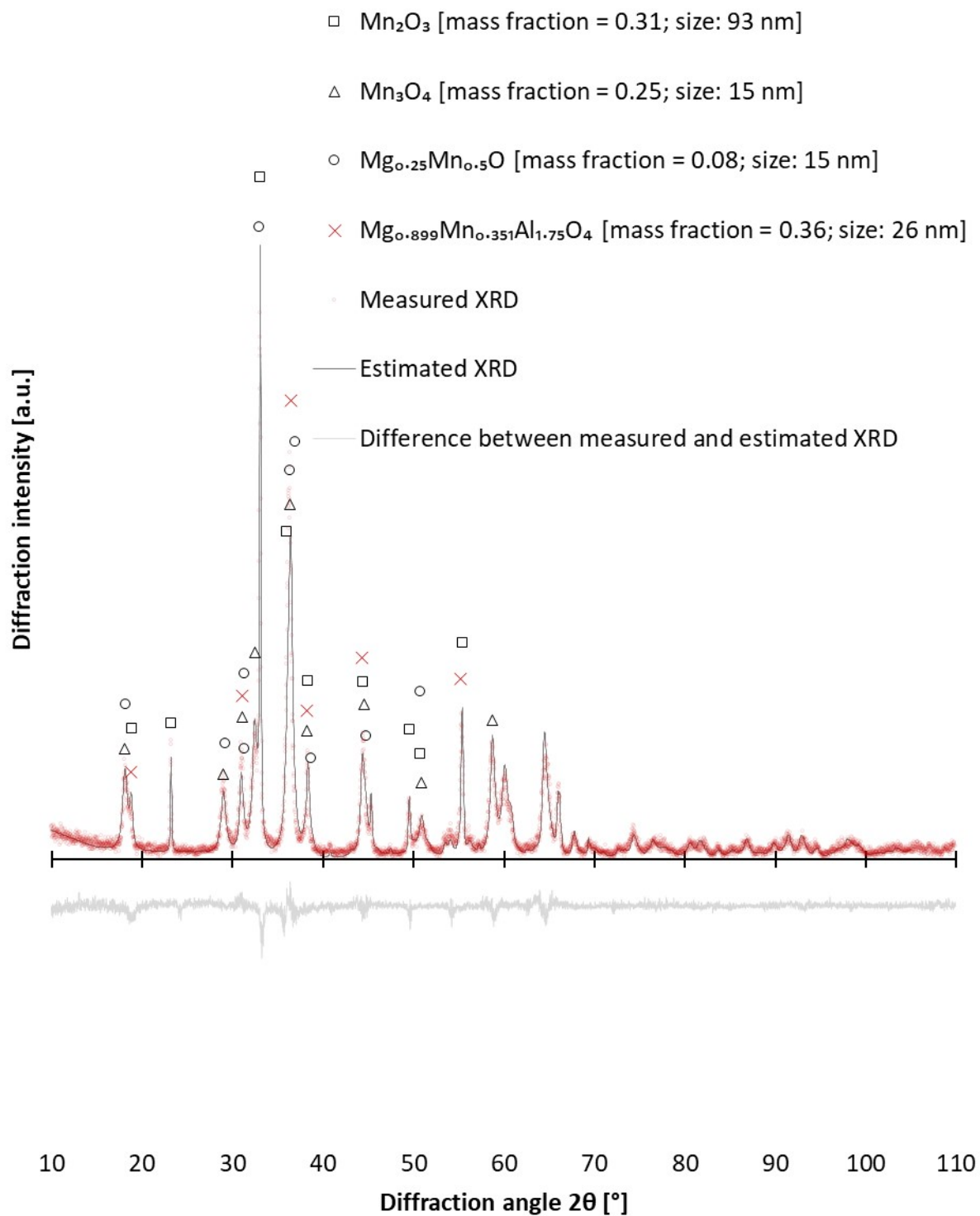


Figure S15: X-ray diffractogram of the fresh oxygen carrier 80% $\text{Mn}_2\text{O}_3/\text{MgAl}_2\text{O}_4$ (in red circles) with the X-ray diffractogram generated by Rietveld refinement (in black) and the difference between the observed and fitted diffractogram (in grey, bottom). Peaks which have an intensity higher than 5% of the maximum peak intensity are marked and identified on the plot.

Table S8: Summary of the results for the Rietveld refinement of different materials and their phases.

Material	Phase	Lattice parameters [10^{-1} nm for a, b, and c or ° for α , β , and γ]						Crystal structure	Space group	Mass fraction	Crystallite size [nm]	Degree of crystallinity [%]	R_{wp}	X^2	Reference
		a	b	c	α	β	γ								
As prepared Fe-based oxygen carrier (Figure S12)	Fe ₂ O ₃	5.027028	5.027028	13.72106	90	90	120	Hexagonal	R -3 c	0.17	59				22
	FeMgAlO ₄	8.269739	8.269739	8.269739	90	90	90	Cubic	F d -3m	0.09	< 3	63.3	0.2774	1.608	23
	Mg _{0.991} Al _{1.917} Fe _{0.08} O ₄	8.151412	8.151412	8.151412	90	90	90	Cubic	F d -3m	0.74	13				24
	CaO	4.809558	4.809558	4.809558	90	90	90	Cubic	F m 3 m	0.53	167				25
As prepared CO ₂ carrier (Figure S13)	CaCO ₃	4.989572	4.989572	17.07212	90	90	120	Hexagonal	R -3 c	0.08	65	80.1	0.2254	1.905	26
	Ca(OH) ₂	3.590446	3.590446	4.916609	90	90	120	Hexagonal	P -3 m 1	0.17	15				27
	CeO ₂	5.406900	5.406900	5.406900	90	90	90	Cubic	F m -3 m	0.22	48				28
After CO ₂ -TPO of oxygen carrier (Figure S14)	Fe ₃ O ₄	8.322095	8.322095	8.322095	90	90	90	Cubic	F d -3m	0.27	126				29
	MgAl ₂ O ₄	8.134712	8.134712	8.134712	90	90	90	Cubic	F d 3 m	0.61	13	73.6	0.2631	1.866	30
	FeAl ₂ O ₄	8.143417	8.143417	8.143417	90	90	90	Cubic	F d 3 m	0.12	53				31
As prepared Mn-based oxygen carrier (Figure S15)	Mn ₂ O ₃	9.356221	9.405141	9.382382	90	90	90	Orthorhombic	P c a b	0.53	167				32
	Mn ₃ O ₄	5.747054	5.747054	9.438224	90	90	90	Tetragonal	I 41/a m d	0.08	65	76.1	0.2424	2.117	33
	Mg _{0.899} Mn _{0.351} Al _{1.75} O ₄	8.169781	8.169781	8.169781	90	90	90	Cubic	F d -3 m	0.17	15				34
	Mg _{0.25} Mn _{0.5} O	5.721406	5.721406	9.298237	90	90	90	Tetragonal	I 41/a m d	0.22	48				35

2.1.4 Temperature programmed reactions

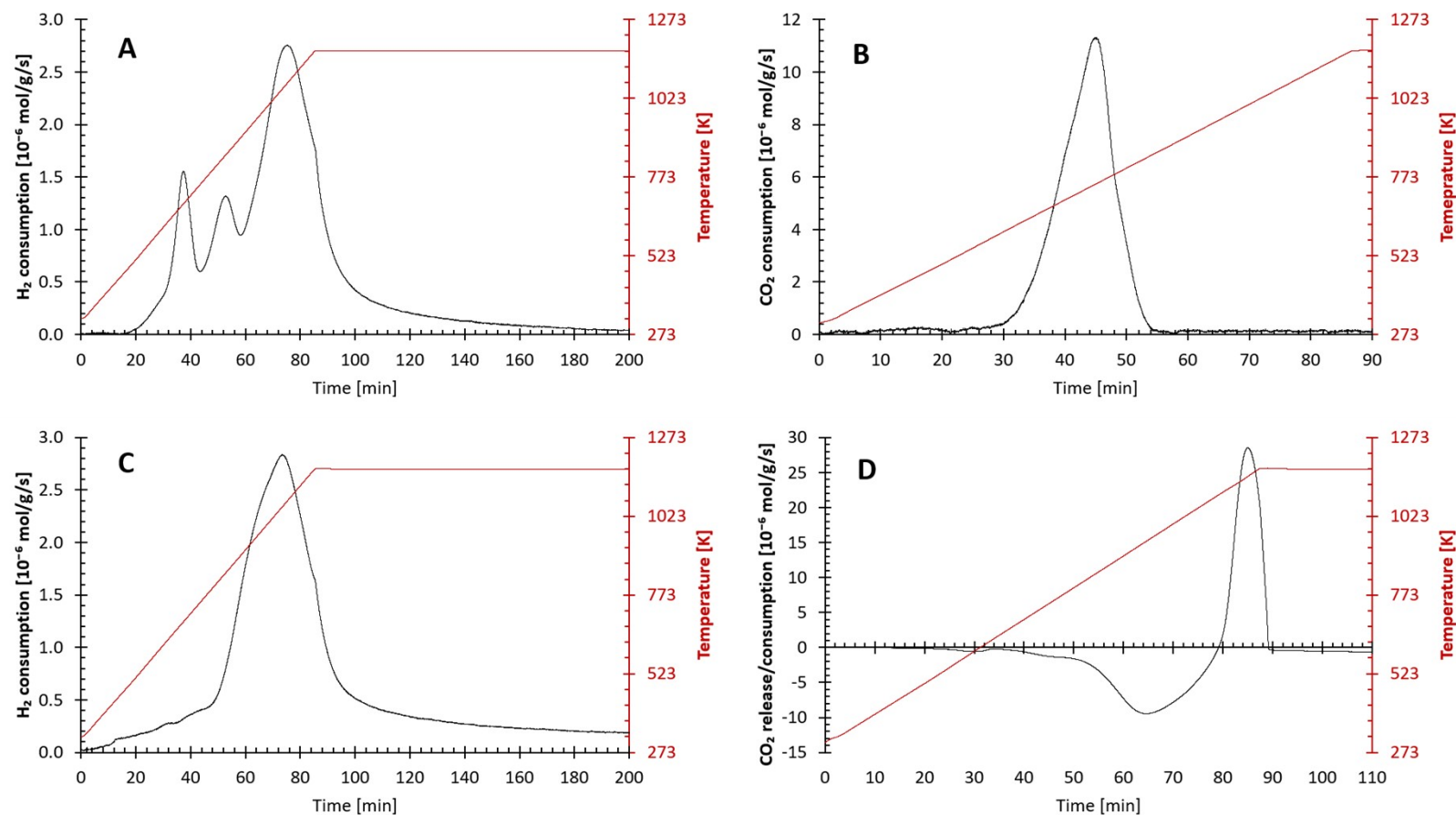


Figure S16: Temperature-programmed reactions (TPRe) with a temperature ramp of 10 K/min up to 1173 K and a total flow rate of $45 \cdot 10^{-6}$ mol/s. A: H₂-TPR under a flow of 5 mol% H₂ in Ar for the determination of exchangeable oxygen atoms in the calcined 50% Fe₂O₃/MgAl₂O₄, the oxygen carrier; B: CO₂-TPO under a flow of 100% CO₂ for the determination of replenishable oxygen atoms in the fully reduced 50% Fe₂O₃/MgAl₂O₄; C: H₂-TPR under a flow of 5 mol% H₂ in Ar for the determination of exchangeable oxygen atoms in the 50% Fe₂O₃/MgAl₂O₄ oxidised by CO₂; D: CO₂-TPCD under a flow of 25% CO₂ in He for the determination of the CO₂ capture and release capacity of the CO₂ carrier, 83% CaO/CeO₂.

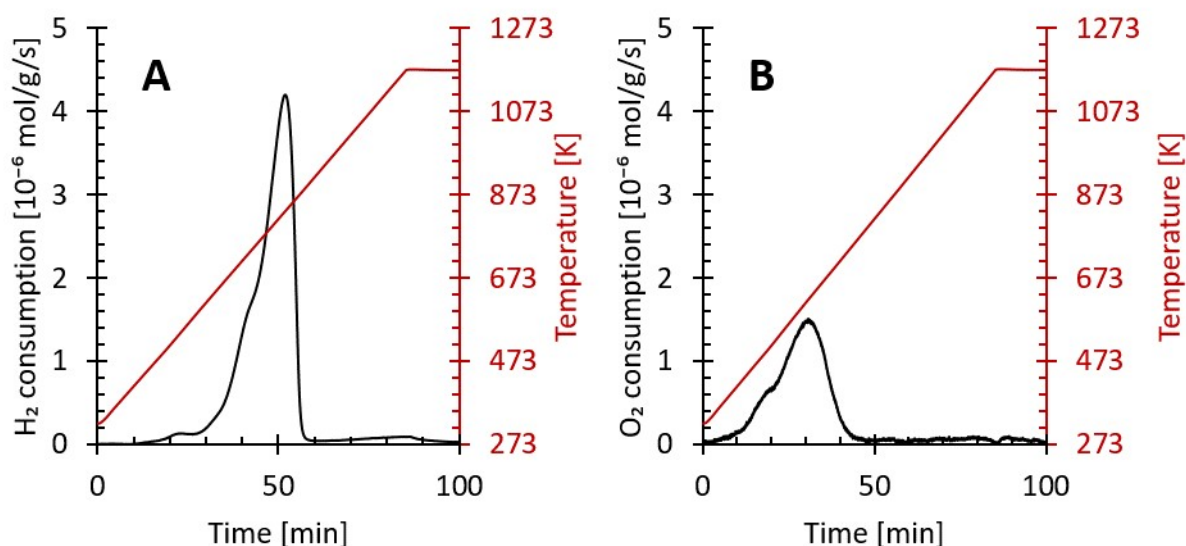


Figure S17: Temperature-programmed reactions (TPRe) with a temperature ramp of 10 K/min up to 1173 K and a total flow rate of $45 \cdot 10^{-6}$ mol/s for the 80% $Mn_2O_3/MgAl_2O_4$. A: H_2 -TPR under a flow of 5 mol% H_2 in Ar for the determination of exchangeable oxygen atoms; B: O_2 -TPO under a flow of 5% O_2 in Ar for the determination of replenishable oxygen atoms in the fully reduced material.

Temperature-programmed reactions were performed in a Micromeritics Autochem II apparatus. For the temperature-programmed reduction (TPR) and temperature-programmed oxidation (TPO), 5% H_2 in Ar and 100% CO_2 or 5% O_2 in Ar were used respectively. For the temperature-programmed carbonation/decarbonation, 25% CO_2 in He was used for 83% CaO/CeO_2 . About 100-150 mg of sample was tested for each material.

Before each experiment, the sample was pre-treated in an inert flow at 623 K to remove adsorbates (for example, water) and then cooled to 323 K. For the temperature-programmed carbonation and decarbonation, the sample was pre-treated in an inert flow at 1173 K to decompose $CaCO_3$ and $Ca(OH)_2$. During the experiments, the temperature was ramped at a rate of 10 K/min. The flow rate was kept constant at $4.5 \cdot 10^{-5}$ mol/s and the pressure was close to 101 kPa. The built-in thermal conductivity detector (TCD) of the setup was used to quantify the amount of gas converted, captured, or released. The TCD was calibrated with a binary gas mixture using 11 different ratios of the two components.

3 Experimental results and data

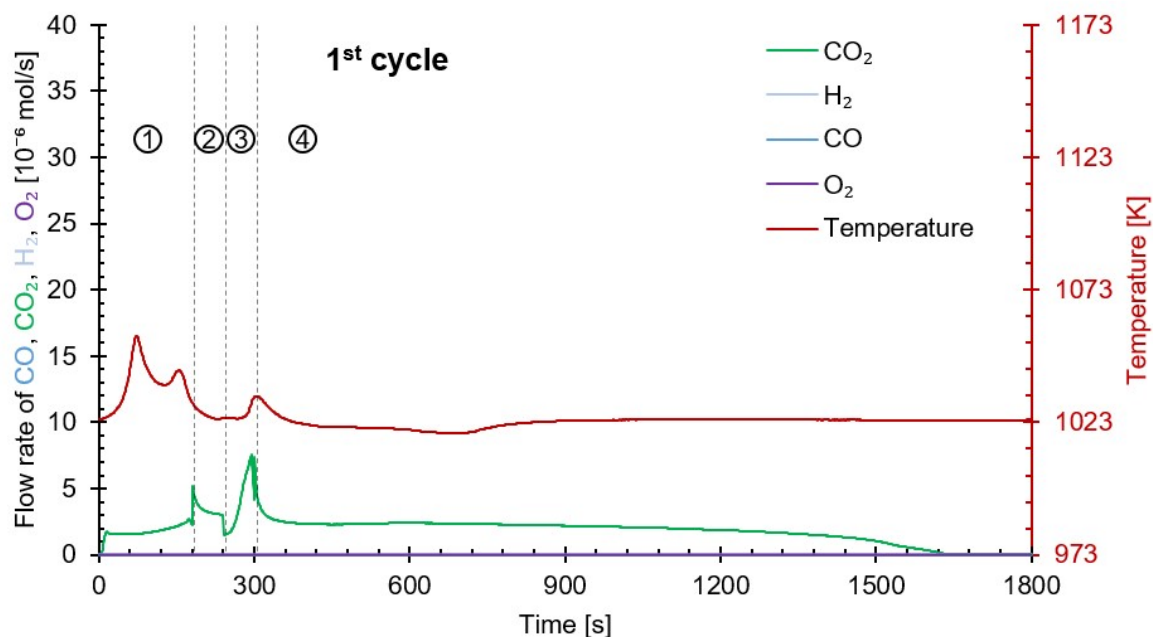


Figure S18: The first of the 30 redox cycles executed for the proof of concept experiments involving Mn₃O₄, CaO, and FeO_x as active materials. Compared to the last 25 cycles, the reduction step lasted 180 seconds instead of 240 cycles to determine the time required for complete decarbonation of the CaCO₃ in the given conditions. The vertical dashed lines indicate the change of stage (from left to right: stages 1 to 4 marked by numbers in circles).

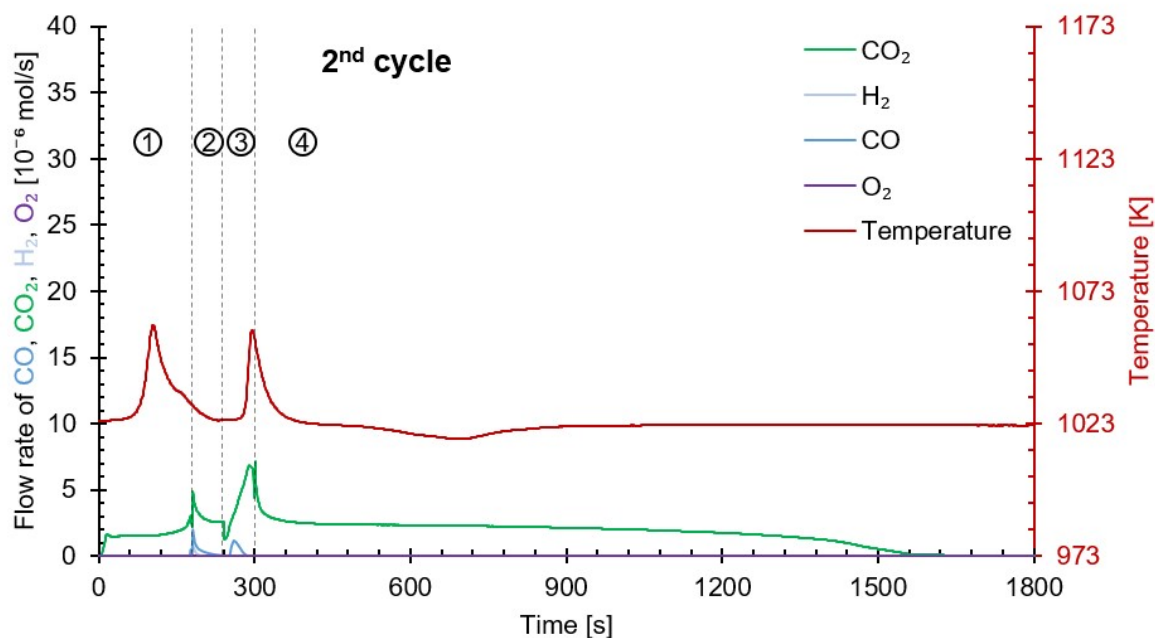


Figure S19: The second of the 30 redox cycles executed for the proof of concept experiments involving Mn₃O₄, CaO, and FeO_x as active materials. Compared to the last 25 cycles, the reduction step lasted 180 seconds instead of 240 seconds. The vertical dashed lines indicate the change of stage (from left to right: stages 1 to 4 marked by numbers in circles).

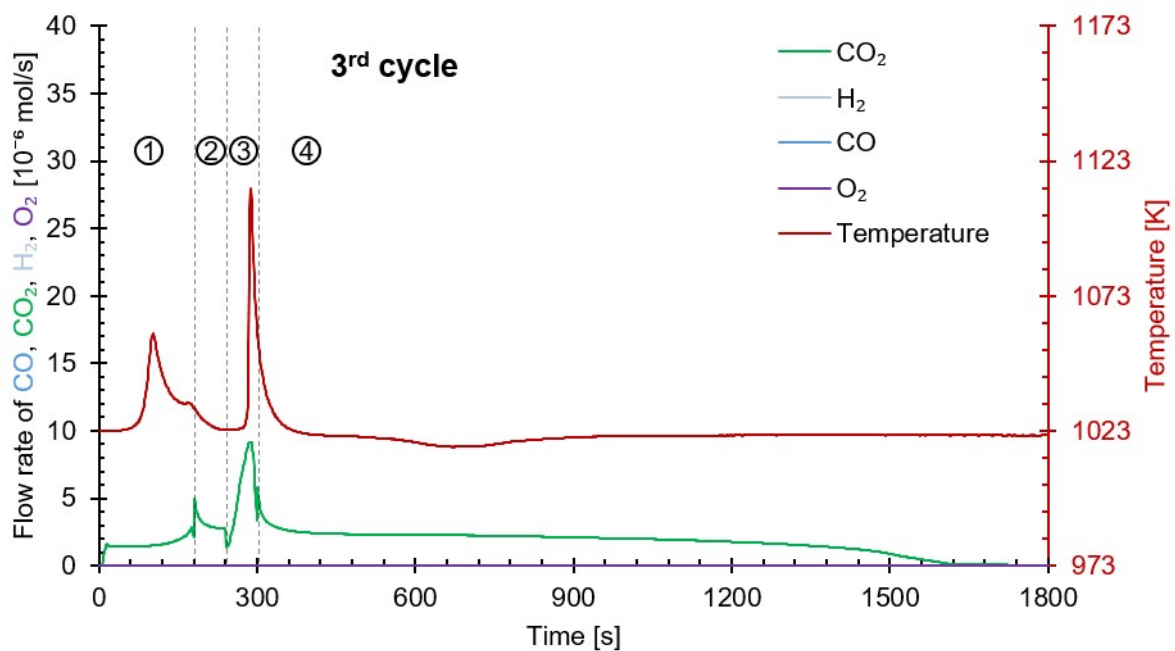


Figure S20: The third of the 30 redox cycles executed for the proof of concept experiments involving Mn₃O₄, CaO, and FeO_x as active materials. Compared to the last 25 cycles, the reduction step lasted 180 seconds instead of 240 seconds. The vertical dashed lines indicate the change of stage (from left to right: stages 1 to 4 marked by numbers in circles).

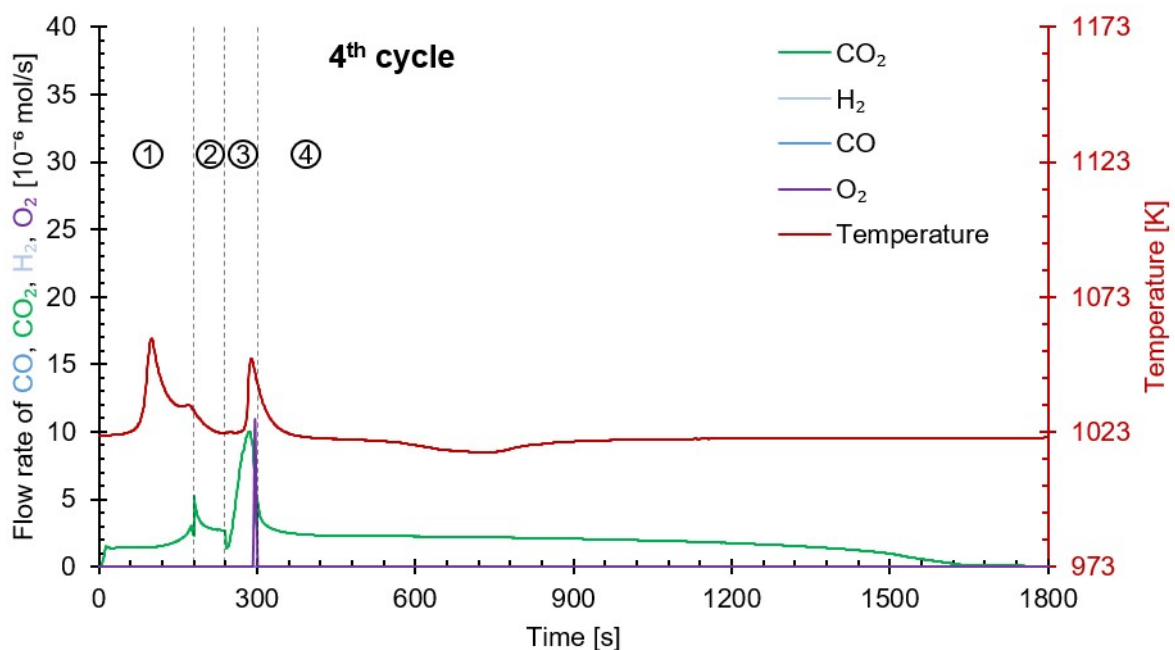


Figure S21: The fourth of the 30 redox cycles executed for the proof of concept experiments involving Mn₃O₄, CaO, and FeO_x as active materials. Compared to the last 25 cycles, the reduction step lasted 180 seconds instead of 240 seconds. The vertical dashed lines indicate the change of stage (from left to right: stages 1 to 4 marked by numbers in circles).

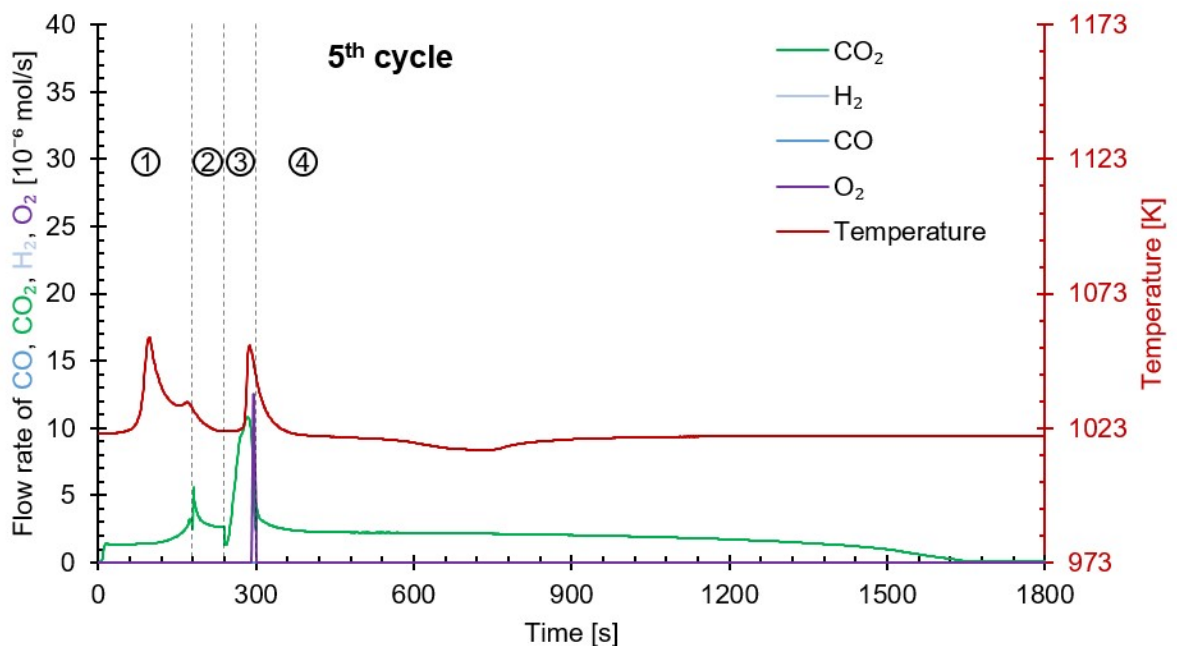


Figure S22: The fifth of the 30 redox cycles executed for the proof of concept experiments involving Mn₃O₄, CaO, and FeO_x as active materials. Compared to the last 25 cycles, the reduction step lasted 180 seconds instead of 240 seconds. The vertical dashed lines indicate the change of stage (from left to right: stages 1 to 4 marked by numbers in circles).

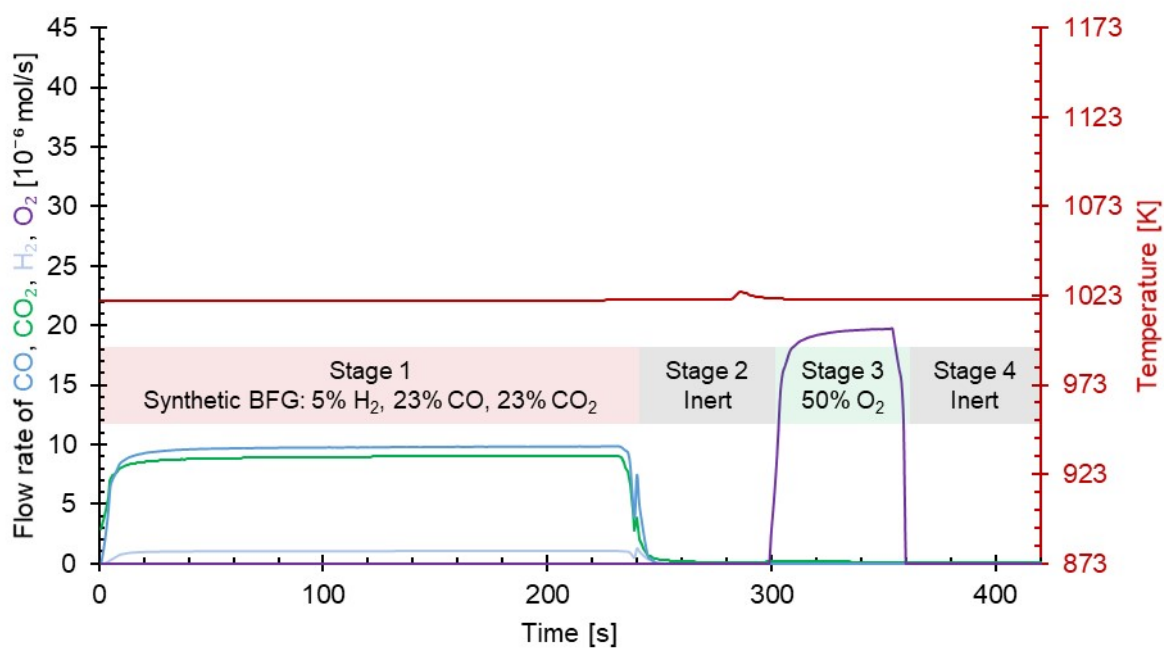


Figure S23: Experimental results showing the outlet flow rates of different components when gases were fed to an empty reactor. Total inlet flow rate during all 4 stages: $41 \cdot 10^{-6}$ mol/s.

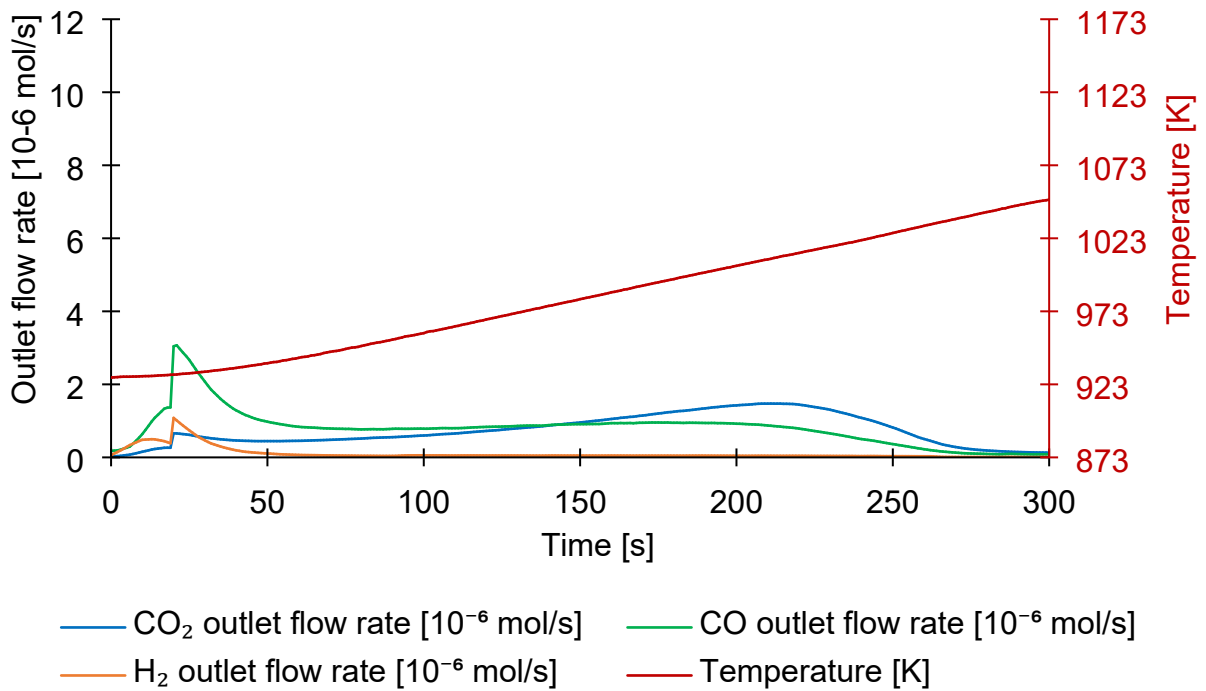


Figure S24: Experimental results of temperature-programmed CO production with shortened reduction-carbonation half-cycle time (20 seconds) and reduction-carbonation carried out at 923 K. Inlet gas flow rate during reduction-carbonation: $41 \cdot 10^{-6}$ mol/s ($10 \cdot 10^{-6}$ mol/s CO; $10 \cdot 10^{-6}$ mol/s CO₂; $2 \cdot 10^{-6}$ mol/s H₂; rest: Ar and He). Inlet gas flow rate during decarbonation-oxidation: $41 \cdot 10^{-6}$ mol/s Ar. Materials were cycled 48 times (isothermally and in temperature-programmed conditions) before the experiment. The reactor bed consisted of approximately 0.5 g of 50% Fe₂O₃/MgAl₂O₄, 0.5 g of 83% CaO/CeO₂, and 1 g of α -Al₂O₃ (as a solid diluent) with a size fraction of 355 – 500 μ m (see Figure S25).



Figure S25: Photos of the reactor containing the solids used for the experiments. The ruler has a cm-based scale.

4 Glossary

Abbreviations

AMU	Atomic mass unit
ASU	Air separation unit
BET	Brunauer-Emmett-Teller
BFG	Blast furnace gas
BJH	Barrett-Joyner-Halenda
CLC	Chemical looping combustion
EDX	Energy dispersive X-ray spectroscopy
GSAS	General structure analysis system
ID	Internal diameter in mm
LCV	Lower calorific value
MFC	Mass flow controller
MS	Mass spectrometer
NIST	National Institute of Standards and Technology, United States of America
PR-BM	Peng-Robinson cubic equation of state with the Boston Matthias alpha function
rWGS	Reverse water-gas shift
SEM	Scanning electron microscope
STEAM-TA	1967 American Society of Mechanical Engineers (ASME) steam tables
TCD	Thermal conductivity detector
TPCD	Temperature-programmed carbonation and decarbonation
TPO	Temperature-programmed oxidation
TPR	Temperature-programmed reduction
TPRe	Temperature-programmed reaction
XRD	X-ray diffraction

Symbols

ΔG	Gibbs free energy of reaction in kJ/mol
ΔH	Enthalpy of reaction in kJ/mol
p	Equilibrium partial pressure
R	Universal gas constant in kJ/mol/K
R_{wp}	Weighted profile R-factor
t	Time of half-cycle in seconds

T Temperature in K
 X^2 Goodness-of-fit

Subscripts

$_0$ At "dead state": 298 K and 101 kPa
 $_{eq}$ At thermodynamic equilibrium

 $_{in}$ Inlet flow in mol/s
 $_{out}$ (Measured) outlet flow in mol/s
 $_{total}$ The total cycle time in seconds
 $_{XK}$ At X K

Superscripts

0 Standard thermodynamic value

References

1. V. K. Shen, D. W. Siderius, W. P. Krekelberg and H. W. Hatch, eds., *NIST Standard Reference Simulation Website*, National Institute of Standards and Technology, Gaithersburg MD, 20899, USA, 2020.
2. C. W. Bale, E. Bélisle, P. Chartrand, S. A. Deckerov, G. Eriksson, A. E. Gheribi, K. Hack, I. H. Jung, Y. B. Kang, J. Melançon, A. D. Pelton, S. Petersen, C. Robelin, J. Sangster, P. Spencer and M. A. Van Ende, *Calphad*, 2016, **54**, 35-53.
3. J. A. Schaidle, S. E. Habas, F. G. Baddour, C. A. Farberow, D. A. Ruddy, J. E. Hensley, R. L. Brutchey, N. Malmstadt and H. Robota, in *Catalysis: Volume 29*, The Royal Society of Chemistry, 2017, vol. 29, pp. 213-281.
4. Vewin, Tarievenoverzicht drinkwater 2020, https://www.vewin.nl/SiteCollectionDocuments/Publicaties/Cijfers/5691-VEW%20Brochure%20Tarievenoverzicht_WEB.pdf, (accessed 13/06/2021, 2021).
5. C.-C. Cormos, *Applied Thermal Engineering*, 2015, **82**, 120-128.
6. F. G. Baddour, L. Snowden-Swan, J. D. Super and K. M. Van Allsburg, *Organic Process Research & Development*, 2018, **22**, 1599-1605.
7. U. S. B. o. L. Statistics, CPI Inflation Calculator, https://www.bls.gov/data/inflation_calculator.htm, (accessed 11/06/2021, 2021).
8. N. V. R. A. Dharanipragada, L. C. Buelens, H. Poelman, E. De Grave, V. V. Galvita and G. B. Marin, *Journal of Materials Chemistry A*, 2015, **3**, 16251-16262.
9. W. Liu, B. Feng, Y. Wu, G. Wang, J. Barry and J. C. D. d. Costa, *Environmental Science and Technology*, 2010, **44**, 3093 - 3097.
10. T. Economics, Manganese Ore, <https://tradingeconomics.com/commodity/manganese>, (accessed 22/06/2021, 2021).
11. R. Anantharaman, O. Bolland, N. Booth, E. van Dorst, C. Ekstrom, E. Sanchez Fernandez, F. Franco, E. Macchi, G. Manzolini, D. Nikolic, A. Pfeffer, M. Prins, S. Rezvani and L. Robinson, *European best practice guidelines for assessment of CO2 capture technologies*, Report D 4.9, Politecnico di Milano – Alstom UK, European Union, 2011.
12. T. Banaszkiwicz, M. Chorowski and W. Gizicki, 2014.
13. W. F. Castle, *International Journal of Refrigeration*, 2002, **25**, 158-172.
14. J. P. Lange, *ChemSusChem*, 2017, **10**, 245-252.
15. K. Z. House, A. C. Baclig, M. Ranjan, E. A. van Nierop, J. Wilcox and H. J. Herzog, *Proceedings of the National Academy of Sciences of the United States of America*, 2011, **108**, 20428-20433.
16. N. Smith, G. Miller, I. Aandi, R. Gadsden and J. Davison, *Energy Procedia*, 2013, **37**, 2443-2452.
17. V. Dieterich, A. Buttler, A. Hanel, H. Spliethoff and S. Fendt, *Energy & Environmental Science*, 2020, **13**, 3207-3252.
18. M. Thommes, K. Kaneko, A. V. Neimark, J. P. Olivier, F. Rodriguez-Reinoso, J. Rouquerol and K. S. W. Sing, *Pure and Applied Chemistry*, 2015, **87**, 1051-1069.

19. W. Wohlleben, J. Mielke, A. Bianchin, A. Ghanem, H. Freiburger, H. Rauscher, M. Gemeinert and V. D. Hodoroaba, *Journal of Nanoparticle Research*, 2017, **19**, 61.
20. A. C. Larson and R. B. Von Dreele, *General Structure Analysis System (GSAS)*, Los Alamos National Laboratory, Los Alamos National Laboratory, 2004.
21. B. H. Toby, *Journal of Applied Crystallography*, 2001, **34**, 210-213.
22. R. L. Blake, R. E. Hessevick, T. Zoltai and L. W. Finger, *American Mineralogist*, 1966, **51**, 123-129.
23. G. E. Bacon and A. J. E. Welch, *Acta Crystallographica*, 1954, **7**, 361-363.
24. F. Martignago, A. D. Negro and S. Carbonin, *Physics and Chemistry of Minerals*, 2003, **30**, 401-408.
25. G. Fiquet, P. Richet and G. Montagnac, *Physics and Chemistry of Minerals*, 1999, **27**, 103-111.
26. D. L. Graf, *American Mineralogist*, 1961, **46**, 1283-1316.
27. L. Desgranges, D. Grebille and G. Calvarin, *Acta Crystallographica Section B*, 1993, **B49**, 812-817.
28. R. W. G. Wyckoff, *Crystal Structures*, Interscience Publishers, New York, USA, 1963.
29. M. E. Fleet, *Acta Crystallographica Section B: Structural Science, Crystal Engineering and Materials*, 1981, **37**, 917-920.
30. S. A. T. Redfern, R. J. Harrison, H. S. C. O'Neill and D. R. R. Wood, *American Mineralogist*, 1999, **84**, 299-310.
31. R. J. Harrison, S. A. T. Redfern and H. S. C. O'Neill, *American Mineralogist*, 1998, **83**, 1092-1099.
32. S. Geller, *Acta Crystallographica Section B*, 1971, **27**, 821-828.
33. V. Baron, J. Gutzmer, H. Rundlof and R. Tellgren, *American Mineralogist*, 1998, **83**, 786-793.
34. F. Bosi, U. Hälenius, G. B. Andreozzi, H. Skogby and S. Lucchesi, *American Mineralogist*, 2007, **92**, 27-33.
35. J. Yin, A. B. Brady, E. S. Takeuchi, A. C. Marschilok and K. J. Takeuchi, *Chemical communications (Cambridge, England)*, 2017, **53**, 3665-3668.